Anisotropic diffusion of concentrated hard-sphere colloids near a hard wall studied by evanescent wave dynamic light scattering

V. N. Michailidou, J. W. Swan, J. F. Brady, and G. Petekidis

Citation: The Journal of Chemical Physics **139**, 164905 (2013); doi: 10.1063/1.4825261
View online: http://dx.doi.org/10.1063/1.4825261
View Table of Contents: http://scitation.aip.org/content/aip/journal/jcp/139/16?ver=pdfcov
Published by the AIP Publishing

Anisotropic diffusion of concentrated hard-sphere colloids near a hard wall studied by evanescent wave dynamic light scattering

V. N. Michailidou,[1] J. W. Swan,[2] J. F. Brady,[2] and G. Petekidis[1,a)]
[1]*FORTH/IESL and Department of Materials Science and Technology, University of Crete, 71110 Heraklion, Greece*
[2]*Division of Chemistry and Chemical Engineering, California Institute of Technology, Pasadena, California 91125, USA*

(Received 8 August 2013; accepted 2 October 2013; published online 28 October 2013)

Evanescent wave dynamic light scattering and Stokesian dynamics simulations were employed to study the dynamics of hard-sphere colloidal particles near a hard wall in concentrated suspensions. The evanescent wave averaged short-time diffusion coefficients were determined from experimental correlation functions over a range of scattering wave vectors and penetration depths. Stokesian dynamics simulations performed for similar conditions allow a direct comparison of both the short-time self- and collective diffusivity. As seen earlier [V. N. Michailidou, G. Petekidis, J. W. Swan, and J. F. Brady, Phys. Rev. Lett. **102**, 068302 (2009)] while the near wall dynamics in the dilute regime slow down compared to the free bulk diffusion, the reduction is negligible at higher volume fractions due to an interplay between the particle-wall and particle-particle hydrodynamic interactions. Here, we provide a comprehensive comparison between experiments and simulations and discuss the interplay of particle-wall and particle-particle hydrodynamics in the self- and cooperative dynamics determined at different scattering wave vectors and penetration depths. © *2013 AIP Publishing LLC*. [http://dx.doi.org/10.1063/1.4825261]

I. INTRODUCTION

A common feature of mesoscopic soft matter systems including biological ones such as cells and biomembranes is the existence of a great number of interfaces which strongly influence the properties of the system and dictate flow mechanisms under confinement.[1,2] The thermal Brownian motion of colloidal particles, polymer chains, and proteins, near a solid or liquid interface, is therefore one of the main subjects in need of understanding in order to be able to predict complex biological functions taking place in such systems. Other examples of biological systems where hydrodynamic interactions have an essential role is the collective motion of sperm cells near an interface,[3] swimming bacteria confined in thin films,[4] as well as during flow and mobility control in biological systems such as protein motion inside cells or through biomembranes. Brownian motion of colloidal particles near surfaces is also of technological importance since its detailed understanding is required for the advancement of microfluidics and optofluidics[5,6] among other applications. Moreover, flows of dilute or concentrated suspensions in confined environments are ubiquitous in industrial processes such as food processing and oil recovery.[7]

Under such confined conditions, near surfaces, interfaces, and in microchannels, particle dynamics are affected both by direct enthalpic interactions[8] as well as excluded volume and hydrodynamic interactions (HI).[9] While the former are system specific and depend on the specific interaction energy between the moving particles/polymers and the surfaces/interfaces, HI are expected to depend generically on the shape, size, and distance of the moving particle from the interface. Furthermore, the knowledge of HI in confinement could in principle be used (or is required) to probe the direct particle/wall interactions via detection of Brownian particle diffusion near a wall. Therefore, a key question is how particle dynamics are affected through HI by the existence of non-penetrable walls.

Different techniques have been used to study near wall dynamics, including evanescent wave dynamic light scattering (EWDLS),[10–16] confocal optical microscopy,[17] total internal reflection microscopy,[18,19] resonance enhanced scattering,[20,21] and laser tweezers.[22] The hydrodynamic interactions between a planar solid surface and a nearby Brownian sphere have been calculated at the level of a single particle as early as the beginning of the 20th century[23] and latter in the 1960s.[24,25] The effect is manifested in the hydrodynamic mobility matrix, **M**, whose components can decrease towards zero when approaching the wall and lead to anisotropic slowing down of the translational, as well as of the rotational diffusion.[26] The theoretical predictions for the diffusion anisotropy parallel and perpendicular to the wall were measured experimentally directly by optical microscopy,[17,27] while in the EWDLS geometry of the translational[28] and more recently the rotational diffusion of a single sphere were also determined.[29] In other confined geometries, the single particle translational diffusion has been measured experimentally[15,27] and calculated by simulations[30] between two walls and in microfluidic channels[31,32] while collective and relative diffusion of two particles near a wall has been studied by microscopy[33–36] and with optical tweezers.[22] At higher particle volume fractions, confinement leads to near wall layering[37] and

a)Author to whom correspondence should be addressed. Electronic mail: georgp@iesl.forth.gr

influences the near wall particle dynamics[16,38] as well as loss of ergodicity.[39]

Evanescent wave dynamic light scattering[10] combines the advantages of dynamic light scattering (DLS), i.e., statistical averaging and fast detection with a localized probing due to the short penetration depth, κ^{-1}, of an evanescent wave that is produced under total internal reflection conditions at an interface.[9] However, the interpretation of the measured intensity time autocorrelation function (TCF), $g^{(2)}(\mathbf{q}, t;\kappa) = \langle I(\mathbf{q}, t;\kappa)I(\mathbf{q}, 0;\kappa)\rangle/\langle I(t)\rangle^2$, is far from trivial as it incorporates both confinement effects and the specific evanescent wave illumination that is decaying exponentially in space away from the solid-liquid interface. In the dilute limit, $g^{(2)}(\mathbf{q}, t;\kappa)$ was originally calculated by Lan *et al.*[10] taking into account the evanescent geometry and the wall mirror effect, while its initial decay incorporating the anisotropic viscous drag effect as a function of distance from the wall was more recently calculated by Holmqvist *et al.*[14,28,40]

With increasing volume fraction (ϕ), particle-particle HIs become important and modify the wall-induced drag effect. In an earlier publication, we studied the Brownian motion of hard-sphere (HS) colloidal particles near a solid, planar surface at volume fractions up to about $\phi = 40\%$.[16] While, as expected in the dilute regime, the diffusion coefficient was found to be slower than the free diffusion in bulk due to the viscous drag effect, we found that the wall-induced reduction of the self-diffusion is negligible at higher volume fractions due to an interplay between the particle-wall and particle-particle hydrodynamic interactions. A simple model captured the basic physical mechanism responsible for such behavior, while a quantitative prediction of the weaker decay of the near-wall self-diffusion coefficient with volume fraction was offered by Stokesian dynamics (SD) simulations.

The results of the above experimental study were also presented in view of a new theoretical formalism describing the EWDLS correlation function and the deduced short-time diffusivities for higher volume fractions.[16] The theory and the extracted short-time self- and collective-diffusivities were also presented in detail for different penetration depths and varying scattering wavevector.[40] A similar theoretical derivation of the initial decay time of the EWDLS correlation function based on a virial expansion was derived by Cichocki *et al.*[41] for moderate non-dilute concentrations, while recently a theoretical analysis of the long-time dynamics in EWDLS was presented for dilute suspensions of spherical particles. The latter was compared favorably with computer simulations and revealed the inaccuracies of the full time-dependent EWDLS correlation function originally deduced by Lan *et al.*[10] that neglected the wall-particle hydrodynamic interactions.

In this work, we extend the experimental and simulation studies in the high volume fraction regime to different scattering wave vectors and penetration depths and provide a comprehensive comparison of the experiments, simulations and theoretical derivation of the short-time dynamics in non-dilute hard sphere suspensions near a wall. The paper is organized as follows: We first present the experimental system and methods. We then describe the theoretical derivation of the near wall diffusivities in the parallel and perpendicular to the wall directions measured via EWDLS. We follow that with a description of the Stokesian dynamics simulations and their analysis. In Sec. IV, we present the experimental results and their comparison with simulation data. Finally, in Sec. V we discuss the findings and present conclusions.

II. SYSTEM AND METHODS

A. Samples

Suspensions of poly(methyl methacrylate) (PMMA) hard spheres with radius $R = 118$ nm or 144 nm (determined by light scattering) were prepared at various volume fractions in a tetralin/cis-decalin (30%/70%) mixture. The solvent mixture was chosen in order to achieve nearly refractive index matching conditions and avoid multiple scattering at high volume fractions. PMMA particles, sterically stabilized by chemically grafted poly-12-hydroxystearic acid (PHSA), is a model system where particles behave as nearly HSs. We prepared several volume fractions by progressively diluting a single batch of concentrated suspension. The volume fraction was determined by measuring the crystal fraction in a suspension at crystal-liquid consistence.[42] The particle volume fraction was varied between $0.002 \leq \phi \leq 0.42$.

B. Dynamic light scattering and evanescent wave dynamic light scattering

We employ conventional DLS and EWDLS to measure, respectively, the 3D and near wall 2D dynamics of HSs at different volume fractions in the dilute and concentrated regime. Both experiments were performed at several scattering wave vectors, q $(= (4\pi n_2/\lambda_0)\sin(\theta_{sc}/2))$, where n_2 $(= 1.497)$ is the suspension refractive index, λ_0 is the laser wavelength, and θ_{sc} is the scattering angle.

Standard light scattering setups (ALV-Germany) for static and dynamic light scattering experiments were used. The instruments were equipped with Nd-Yag laser ($\lambda_0 = 532$ nm, FORTH, Crete) or a helium-neon laser ($\lambda_0 = 632.8$ nm, Forschungszentrum Juelich). The intensity time autocorrelation function is recorded by an ALV-5000 multi-tau digital correlator. The samples were thermostated in a cell with temperature stability of $\pm 0.1\,^{\circ}$C.

Two different EWDLS setups were used enabling us to probe different q scans as described below. In both cases, the evanescent wave was generated at the interface of a semi-cylindrical prism of high refractive index, n_1, with the suspending liquid confined in a cell attached to the prism. Under conditions of total internal reflection, the penetration depth is $2/\kappa = [(2\pi/\lambda_0)\sqrt{(n_1 \sin\theta_i)^2 - n_2^2}]^{-1}$, where θ_i is the angle at which the incident beam impinges on the interface.

We measured the time-dependent light scattering intensity, $I(\mathbf{q}, t;\kappa)$, and computed the normalized intensity TCF,[42] $g^{(2)}(\mathbf{q}, t;\kappa)$, at room temperature ($T = 18\,^{\circ}$C), under homodyne (for the DLS) or mixed homodyne-heterodyne conditions due to the strong static scattering from the prism surface (for the EWDLS) that moreover varies from speckle to speckle and with θ_{sc} and κ. We then calculate the normalized field auto-correlation function (or intermediate

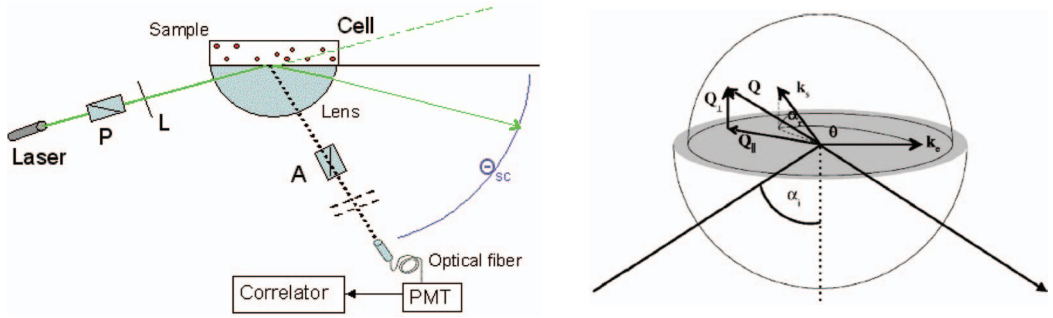

FIG. 1. Schematic of the two EWDLS setups used: (a) EWDLS1 (FORTH, Crete), where the perpendicular and parallel components of q are changed simultaneously and (b) EWDLS2 (Forschungszentrum Juelich) setup for independent quasi-parallel and quasi-perpendicular scans.

scattering function), $f(\mathbf{q}, t; \kappa) = \langle E(\mathbf{q}, t; \kappa) E^{\dagger}(\mathbf{q}, 0; \kappa) \rangle / \langle I \rangle$ from $g^{(2)}(\mathbf{q}, t; \kappa)$, using the usual Siegert relation for conventional 3D data, $g^{(2)}(\mathbf{q}, t; 0) = 1 + [f(\mathbf{q}, t; 0)]^2$ or the modified Siegert relation[14] for EWDLS data. In both cases, we further compute the initial decay rate of the correlation function,[42] $\Gamma = -\frac{\partial}{\partial t} \ln f(\mathbf{q}, t; \kappa)$ as $t \to 0$, to determine the q-dependent short-time diffusion coefficient, $D(\phi, \mathbf{q}) = \Gamma / q^2$.

In this work, we have utilized two different EWDLS setups:

(A) A colloidal suspension of PMMA HS particles with radius $R = 118$ nm was used with a two axis goniometer (EWDLS1 at FORTH, Crete, Figure 1(a)). The sample cell was placed at the center of the goniometer that allowed variation of q (in the range $1 < qR < 7$) using a Nd-Yag laser with $\lambda_0 = 532$ nm with a power of 150 mW. The evanescent wave was generated at the interface of a semi-cylindrical prism of high refractive index ($n_1 = 1.627$) with the suspending liquid confined in a cell attached to the prism with the electric field penetration depth $2/\kappa = [(2\pi n_1/\lambda_0)\sqrt{\sin^2\theta_i - \sin^2\theta_c}]^{-1}$, where $\theta_c = 67.9^{\circ}$ the measured critical angle. Here, the penetration depth chosen was $2/\kappa = 321$ nm corresponding to $\kappa R = 0.735$.

(B) A similar colloidal suspension with particles of radius $R = 144$ nm was used in a triple axis goniometer (EWDLS2 at Forschungszentrum Juelich, Figure 1(b)) with a spherical sample cell to construct a scattering geometry as shown in Figure 1(b). The cell consists of a massive SF10-glass semispherical lens ($n_1 = 1.723$) covered by a dome, which contains the sample solution. The incident beam is totally reflected from the interface between the bottom part and the solution if the angle of incidence, α_i, is larger than the critical angle of total reflection $\alpha_c = 29.5^{\circ}$. Since we can change the observation angle in-plane θ and off-plane α_r, $q_{\perp} = (2\pi/\lambda)\sin\alpha_r$ can be changed while $q_{\parallel} = (2\pi/\lambda)\sqrt{1 + \cos^2\alpha_r - 2\cos\alpha_r \cos\theta}$ is kept constant and vice versa, with the total scattering vector magnitude given by $q = \sqrt{q_{\parallel}^2 + q_{\perp}^2}$. Here, the illuminating beam was generated by a He-Ne laser with a power of 35 mW and $\lambda_0 = 632.8$ nm, which is mounted on the source arm of the triple axis goniometer. Varying the angle of incidence, the penetration depth can be changed approximately in the range 100 nm $\leq 2/\kappa \leq 1000$ nm. The upper limit is mainly set by focusing of the incoming beam in the bottom part of the sample cell and the divergence of the penetration depth at the critical angle. During a parallel scattering wavevector, $q_{\parallel}$, scan, θ is changed within $0^{\circ} \leq \theta \leq 120^{\circ}$ keeping $\alpha_r = 60^{\circ}$. On the other hand, during a quasi-perpendicular scattering wavevector, $q_{\perp}$, scan, both θ and α_r are changing in such a way that $q_{\parallel}$ is constant. Here, we used a penetration depth of $2/\kappa = 219$ nm corresponding to $\kappa R = 1.315$.

III. THEORY AND SIMULATIONS

The scattered intensity measured experimentally by a photomultiplier tube (PMT), usually at a single speckle (coherence area), fluctuates around a mean value, $\langle I \rangle$, so that $\langle I(\mathbf{q}, t) I(\mathbf{q}, 0) \rangle = \langle I(0) \rangle^2 + \langle \delta I(\mathbf{q}, t) \delta I(\mathbf{q}, 0) \rangle$, where the second term gives the time dependence of the concentration fluctuations in our suspension. So $\langle \delta I(\mathbf{q}, t) \delta I(\mathbf{q}, 0) \rangle / \langle I(0) \rangle^2 = g^{(2)}(\mathbf{q}, t) - 1$ which, in the Gaussian approximation (i.e., the scattered field follows the Gaussian distribution), is equal to $|g^{(1)}(\mathbf{q}, t)|^2 = |\langle E(\mathbf{q}, t) E^*(\mathbf{q}, 0) \rangle / \langle I(0) \rangle|^2$. This relation between the field correlation function and the intensity correlation function is known as the Siegert relation and in most cases holds (except, for example, when there are few scatterers in the scattering volume that result in significant number fluctuations).[43] The normalized scattered field correlation function, $g^{(1)}(\mathbf{q}, t)$, is essentially the intermediate scattering function $f(\mathbf{q}, t) = \langle \sum_{i,j=1}^{N} e^{i\mathbf{q}\cdot\mathbf{r}_i(t) - i\mathbf{q}\cdot\mathbf{r}_j(0)} \rangle = \langle \delta\rho(\mathbf{q}, t) \delta\rho(\mathbf{q}, 0) \rangle$ for $q \neq 0$ with $\delta\rho(\mathbf{q}, t)$ the Fourier transform of the particle density, $\rho(\mathbf{r}, t) = \rho_0 + \delta\rho(\mathbf{r}, t)$, which provides information on the dynamics of concentration fluctuations.

A. EWDLS diffusivity

The evanescent wave dynamic light scattering measurements involve some constraints due to the existence of the hard wall and the evanescent wave illumination. Consider a suspension of particles of hydrodynamic radius R with average volume fraction ϕ and at temperature T residing above

a stationary, no-slip plane wall with normal $\mathbf{e}_3$. When the Reynolds number, UR/ν, where U is a characteristic velocity and ν is the kinematic viscosity of the solvent, describing the relative importance of viscous drag and inertia is small, the resistance to motion of particles through the fluid is linearly proportional to the particle velocities. The coefficient of proportionality divided by the solvent viscosity η is strictly a function of the particle geometry (i.e., particle size and shape, relative particle positions and the positions of the particles relative to the wall). This coefficient of proportionality is written as $\mathbf{M}$ – the many-particle hydrodynamic mobility.

When a laser impinges on the boundary between two media such that it is totally reflected, the continuity of electric polarizability generates an evanescent wave in the reflective medium which is characterized by the evanescent penetration depth $2/\kappa$. The intensity of this wave decays exponentially with respect to distance from the interface and κ modulates the decay rate. Because of the coherent character of laser illumination, the total electric field of scattered evanescent beam $E(\mathbf{q}, t; \kappa)$, is a linear superposition of those scattered by the N individual particles,

$$E(\mathbf{q}, t; \kappa) = \sum_{\alpha=1}^{N} E_0 e^{-\frac{\kappa}{2}\mathbf{e}_3\cdot\mathbf{x}_\alpha(t)+i\mathbf{q}\cdot\mathbf{x}_\alpha(t)} = \sum_{i=1}^{N} E_0 e^{i\mathbf{k}\cdot\mathbf{x}_\alpha(t)}, \quad (1)$$

where $\mathbf{x}_\alpha(t)$ is the center of mass position of particle α at time t and $\mathbf{k}$ is a complex wave vector

$$\mathbf{k} = \mathbf{q} + i\frac{\kappa}{2}\mathbf{e}_3, \quad (2)$$

with its conjugate denoted as $\bar{\mathbf{k}}$. This effective wave vector is especially convenient in connecting the light scattering experiments to the dynamics of the suspension. It also corresponds to one particularly interesting interpretation of evanescent waves – that unlike direct light scattering, the wave vector contains a complex component. This allows the problem of scattering from evanescent waves to be recast into the conventional light scattering construction. In the usual fashion, the auto-correlation of the scattered field among all scatters is denoted $f(\mathbf{q}, t; \kappa)$, while that for self-scattering is denoted $f_S(\mathbf{q}, t; \kappa)$. These are the intermediate and self-intermediate scattering functions, respectively. As outlined in Ref. 16 and presented in detailed in Ref. 40, the wave vector dependent diffusivity, denoted $D_{2D}(\phi, \mathbf{q}, \kappa)$, is given by

$$\begin{aligned} D_{2D}(\phi, \mathbf{q}, \kappa) &= -\frac{1}{\mathbf{k}\cdot\bar{\mathbf{k}}}\frac{\partial}{\partial t}\log f(\mathbf{q}, t\to 0; \kappa) \\ &= -\frac{1}{(N-1)!\, f(\mathbf{q}, 0; \kappa)} \\ &\quad \times \int \mathbf{k}\cdot\left[\mathbf{D}_{11} + (N-1)\mathbf{D}_{21} e^{i\mathbf{k}\cdot(\mathbf{x}_2(0)-\mathbf{x}_1(0))}\right] \\ &\quad \cdot \mathbf{k}\, e^{-\kappa\mathbf{e}_3\cdot\mathbf{x}_1(0)} P_N^0(\mathbf{x}^N(0))\, d\mathbf{x}^N(0), \end{aligned} \quad (3)$$

where $\mathbf{D}_{11}$ and $\mathbf{D}_{21}$ are the product of the self- and pair-hydrodynamic mobilities and the thermal energy kT, respectively, while $P_N^0(\mathbf{x}^N(0))$ denotes the initial probability distribution of particles. One can see clearly that varying the wave-vector allows the determination of the components of the diffusivity both parallel and perpendicular to the plane wall. This expression can be reduced to more familiar diffusive quantities by limiting the value of the wave vector and assuming that both the probability distribution and the hydrodynamic mobility are transversely isotropic.

In the limit that the wave vector is large, this reduces to the short-time self-diffusivity, viz.,

$$\begin{aligned} D_0^S(\phi, \mathbf{q}, \kappa) &= -\frac{1}{\mathbf{k}\cdot\bar{\mathbf{k}}}\frac{\partial}{\partial t}\log f_S(\mathbf{q}, t\to 0; \kappa) \\ &= \frac{q_\parallel^2 D_\parallel^S + \left(q_\perp^2 + \frac{\kappa^2}{4}\right) D_\perp^S}{q_\parallel^2 + q_\perp^2 + \frac{\kappa^2}{4}}, \end{aligned} \quad (4)$$

where the components of the wave vector parallel and perpendicular to the wall are defined as $\mathbf{q}\cdot\mathbf{q} = q_\parallel^2 + q_\perp^2$, $q_\perp = \mathbf{q}\cdot\mathbf{e}_3$, and

$$D_\parallel^S(\phi, \kappa) = \frac{\int \mathbf{D}_{11} : \mathbf{e}_1\mathbf{e}_1 e^{-\kappa\mathbf{e}_3\cdot\mathbf{x}_1(0)} P_N^0(\mathbf{x}^N(0))\, d\mathbf{x}^N(0)}{\int e^{-\kappa\mathbf{e}_3\cdot\mathbf{x}_1(0)} P_N^0(\mathbf{x}^N(0))\, d\mathbf{x}^N(0)}, \quad (5)$$

$$D_\perp^S(\phi, \kappa) = \frac{\int \mathbf{D}_{11} : \mathbf{e}_3\mathbf{e}_3 e^{-\kappa\mathbf{e}_3\cdot\mathbf{x}_1(0)} P_N^0(\mathbf{x}^N(0))\, d\mathbf{x}^N(0)}{\int e^{-\kappa\mathbf{e}_3\cdot\mathbf{x}_1(0)} P_N^0(\mathbf{x}^N(0))\, d\mathbf{x}^N(0)}. \quad (6)$$

Note that the component of the parallel diffusivity is written in terms of one of parallel dyad of $\mathbf{D}_{11}$ ($\mathbf{e}_1\mathbf{e}_1$) but could be written in terms of the other ($\mathbf{e}_2\mathbf{e}_2$) without affecting the average. This result again matches with that of Holmqvist *et al.*,[14] but the diffusivities parallel and perpendicular to the wall are now averaged over the positions of all the particles and not just the scattering test particle. In the dilute limit, $\phi \to 0$, the initial probability density $P_N^0(\mathbf{x}^N(0))$ is such that the positions of all the particles are completely uncorrelated, subject to the requirement that the particles must reside above the plane wall. We are not restricted to this limit however, and the above expression is valid over the entire range of volume fractions and thus we can probe the short-time self-diffusivity of a particle at any volume fraction.

Similarly, in the limit of the small wave vector, the collective diffusivity is recovered, viz.,

$$D_0^C(\phi, \kappa) = \frac{\int \left[\mathbf{D}_{11} e^{-\kappa\mathbf{e}_3\cdot\mathbf{x}_1(0)} + (N-1)\mathbf{D}_{21} e^{-\frac{\kappa}{2}\mathbf{e}_3\cdot(\mathbf{x}_2(0)+\mathbf{x}_1(0))}\right] : \mathbf{e}_3\mathbf{e}_3 P_N^0(\mathbf{x}^N(0))\, d\mathbf{x}^N(0)}{\int \left[e^{-\kappa\mathbf{e}_3\cdot\mathbf{x}_1(0)} + (N-1) e^{-\frac{\kappa}{2}\mathbf{e}_3\cdot(\mathbf{x}_2(0)+\mathbf{x}_1(0))}\right] P_N^0(\mathbf{x}^N(0))\, d\mathbf{x}^N(0)}, \quad (7)$$

which measures the collective hydrodynamics of a suspension but only in the direction normal to the wall. The evanescent wave is unable to recover information about the parallel wall collective dynamics in the zero scattering wave vector limit because the decaying intensity of the scattered wave screens out the correlation of any in-plane density fluctuations. Effectively, the averaged hydrodynamics parallel to the wall are $O(\mathbf{q})$ and small, and so they make no measurable contribution as they are overwhelmed by perpendicular fluctuations. The collective diffusivity measured by evanescent wave spectroscopy is a sum of the self-diffusivity contribution ($\mathbf{D}_{11}$) weighted exponentially by the distance of a single particle from the wall and the inter-particle contribution ($\mathbf{D}_{21}$) weighted exponentially by the mean distance of any two particles from the wall. In the limit that $\kappa \to 0$, it is clear that indeed, the typical collective diffusivity is recovered as expected.

Equations (5)–(7) are the EWDLS statistical averages equivalent to conventional DLS represented by the ratio of a hydrodynamic quantity, here the weighted average $\mathbf{D}$, to a thermodynamic quantity, which here is the near wall structure factor, $f(\mathbf{q}, 0; \kappa)$. The main characteristic of these expressions, which are valid for all volume fractions, is the exponential averaging introduced by the decay of the evanescent wave away from the wall (see also Refs. 16 and 40).

B. Calculation of the wave vector dependent diffusivity

For the calculation of the wave vector dependent diffusivities (Eqs. (5)–(7)), we suppose that each particle j among N particles is subject to the force

$$\mathbf{F}_j = e^{i\mathbf{k}\cdot\mathbf{x}_j}\mathbf{k}. \tag{8}$$

One can show[40] that the wave vector dependent diffusivity can be expressed as

$$D_{2D}(\phi, \mathbf{q}, \kappa) = kT \frac{\langle \mathbf{F} \cdot \mathbf{M} \cdot \bar{\mathbf{F}} \rangle}{\left\langle \left(\sum_{i,j} \mathbf{F}_i \cdot \bar{\mathbf{F}}_j \right) \right\rangle}, \tag{9}$$

where the angle brackets denote an ensemble average over particle configurations, $\mathbf{F}$ and $\bar{\mathbf{F}}$ are the $3N$ component total force vector and its complex conjugate. This expression is valid for any system geometry, though in this study the hydrodynamic mobility of an assortment of particles in a parallel wall channel is used. In this way, the specific $D_{\parallel}^{S}(\phi, \kappa)$, $D_{\perp}^{S}(\phi, \kappa)$, and $D_{0}^{C}(\phi, \kappa)$ were calculated choosing $\mathbf{F}_j$ appropriately in the direction parallel or perpendicular to the wall, as discussed in more detail in Ref. 40.

C. Stokesian dynamics simulations in confinement

The computation of $\mathbf{M}$ is the chief purpose of accelerated Stokesian dynamics simulations.[44] As demonstrated by Swan and Brady,[32] the velocities of particles bound in a channel and subjected to an arbitrary body force, $\mathbf{f}$, can be computed via direct solution of the Stokes equations:

$$\eta \nabla^2 \mathbf{u} = \nabla p - \mathbf{f}, \tag{10}$$

where $\mathbf{u}$ and p are the solvent velocity and pressure. This solution is split into two additive pieces that characterize the local and global effects of the body force and which can be computed rapidly in real and reciprocal space, respectively. The description of the body force is such that it reflects a specified set of force moments about each of the particles (i.e., force, torque, stresslet, etc.). When this set of moments is truncated (here at the stresslet level), the solution is independently unable to capture the behavior of the particles in cases where two surfaces (particle-particle or particle-wall) are nearly touching – the so-called lubrication regime. Because of this, the set of truncated force moments are often termed far-field forces. One can restore the lubrication effects by searching for the unique set of far-field force moments that produce rigid body motion among the particles and is self-consistent with the dynamics characterized by the known and exact lubrication interactions. The details of how one imposes this constraint are beyond the purview of this paper, but this is discussed at length by Durlofsky, Brady, and Bossis[45] and again by Sierou and Brady[44] and in the case of bound suspensions by Swan and Brady.[32]

D. System in SD simulations

Simulations were performed for different volume fractions up to 42% using a channel of 20 particle radii in width. The systems contained typically 2000 particles and the presented results are the average of several realizations (about 50) in order to improve statistics both in the measured hydrodynamic part, $H(\phi, \mathbf{q}, \kappa)$, and the static structure factor $S(\mathbf{q})$. The initial particle configurations were created through a Monte Carlo simulations, by placing particles randomly in the channel at the desired volume fraction and subsequent equilibration of the system via a molecular dynamics scheme.[46] The width of the channel is large enough so that no effect of the second boundary is introduced both in the statics and the dynamics; therefore, the current simulation is appropriate for comparing with the experimental systems which consists of a single boundary wall.

The EWDLS diffusion coefficients were determined by SD simulations according to the above procedure for different scattering wavevectors and for the specific parallel and quasi-perpendicular scans performed experimentally. Since the aim of the current work is to closely compare experiments and simulations, we present data at two volume fractions in the semidilute and more concentrated regime, i.e., at $\phi = 0.25$ and $\phi = 0.42$ for the penetration depth conditions of the experiment.

IV. RESULTS AND DISCUSSION

In Figure 2, we show correlation functions in the dilute regime, $\phi = 0.05$, from near wall EWDLS measurements and conventional bulk DLS. Data are presented for two scattering wave vectors, q, a high one ($q = 0.02792\ \text{nm}^{-1}$, Figure 2(a)) and an intermediate one ($q = 0.0149\ \text{nm}^{-1}$, Figure 2(b)). The EWDLS measurements were performed with the EWDLS2 setup where $q_{\perp}$ and $q_{\parallel}$ can be changed independently as

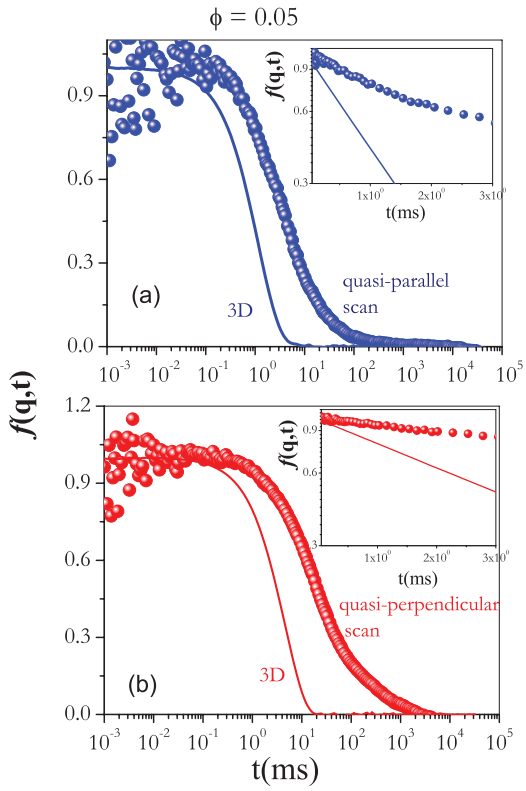

FIG. 2. Intermediate scattering functions, $f(\mathbf{q}, t;\kappa)$ from EWDLS2 (filled symbols) with $2/\kappa = 219$ nm ($\kappa R = 1.315$) and conventional DLS (3D, $\kappa = 0$, solid lines), for a dilute suspension with $\phi = 0.05$: (a) At high total $q = 0.02792$ nm^{-1} (bulk) and $q = 0.02796$ nm^{-1}, $q_{\parallel} = 0.02339$ nm^{-1}, $q_{\perp} = 0.001531$ nm^{-1} (quasi-parallel scan in EWDLS2), (b) at intermediate total $q = 0.01486$ nm^{-1} (bulk) and $q = 0.01506$ nm^{-1}, $q_{\parallel} = 0.00884$ nm^{-1}, $q_{\perp} = 0.01129$ nm^{-1} (quasi-perpendicular scan in EWDLS2). Insets show the initial decay of the same data.

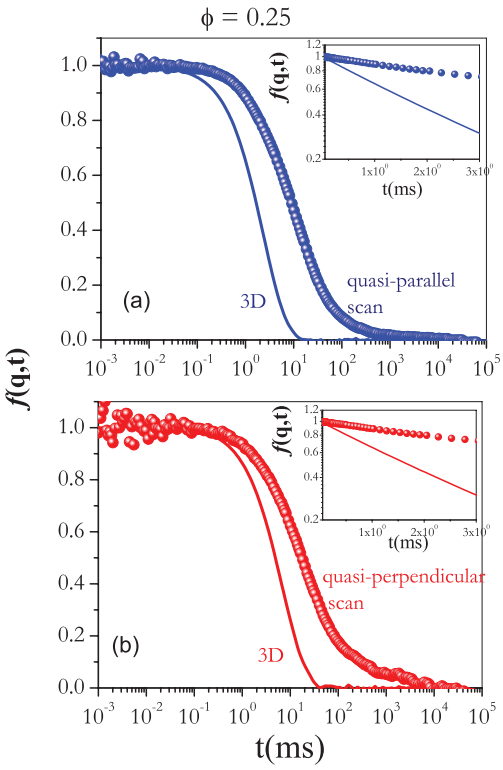

FIG. 3. Intermediate scattering functions, $f(\mathbf{q}, t;\kappa)$ from EWDLS2 (filled symbols) with $2/\kappa = 219$ nm ($\kappa R = 1.315$) and conventional DLS (3D, $\kappa = 0$, solid lines), for an intermediate concentration, $\phi = 0.25$: (a) At high total $q = 0.02792$ nm^{-1} (bulk) and $q = 0.02796$ nm^{-1}, $q_{\parallel} = 0.02339$ nm^{-1}, $q_{\perp} = 0.001531$ nm^{-1} (quasi-parallel scan in EWDLS2), (b) at intermediate total $q = 0.01486$ nm^{-1} (bulk) and $q = 0.01506$ nm^{-1}, $q_{\parallel} = 0.00884$ nm^{-1}, $q_{\perp} = 0.01129$ nm^{-1} (quasi-perpendicular scan in EWDLS2). Insets show the initial decay of the same data.

described above. In Figure 2(a), we compare the EWDLS correlation function from a quasi-parallel scan measurement with $q_{\perp} = 0.0153$ nm^{-1} and $q_{\parallel} = 0.0234$ nm^{-1}, giving a total $q = 0.02796$ nm^{-1}, very close to the q value in the bulk. Similarly in Figure 2(b), we present an EWDLS correlation function from a quasi-perpendicular scan with $q_{\perp} = 0.01129$ nm^{-1} and $q_{\parallel} = 0.00884$ nm^{-1} giving a $q = 0.01506$ nm^{-1} and compare it with a bulk measurement with $q = 0.0149$ nm^{-1}.

As expected due to hydrodynamic effects, the near wall dynamics are significantly slowed down compared to the bulk both at high and low q. Such slowing down is better seen in a log-linear plot of the short-time dynamics in the insets of Figures 2(a) and 2(b). Moreover, at longer times the near wall dynamics exhibit an additional long-time tail, or a second slow relaxation, introduced both by the EWDLS illumination as well as confinement effects. In the dilute limit, such long-time EWDLS tails have been detected in most previous EWDLS measurements[10,11,16,47] although they are still not well understood. At the level of short and intermediate time scales, the EWDLS correlation function has been discussed both in the absence of hydrodynamic interactions in the early EWDLS studies[10] as well as more recently using computer simulations that take into account hydrodynamic interactions.[47]

We now present a comparison of the near wall EWDLS with bulk 3D measurements for a more concentrated suspension. In Fig. 3, we show data at $\phi = 0.25$, with similar $q_{\perp}$ and $q_{\parallel}$ values as in the dilute case of Figure 2. Near wall dynamics are again slower than in the bulk, although they start approaching each other, in agreement with earlier studies by Michailidou *et al.*[16] at similar ϕ. According to experiments and computer simulations presented in Ref. 16, the near wall dynamics approach the bulk dynamics with increasing volume fraction and become almost identical for $\phi \geq 0.3$, due to a balance of the wall-particle HI by the particle-particle HI which becomes progressively stronger as ϕ is increased. We should also point out that the data presented in Figure 3 were taken with a significantly shorter penetration depth ($2/\kappa = 219$ nm or $\kappa R = 1.315$) and therefore wall-particle HIs are much stronger and not yet masked in contrast to what was observed in Ref. 16 (with $2/\kappa = 800$ nm or $\kappa R = 0.458$) where EWDLS and bulk dynamics were almost indistinguishable at volume fractions as low as $\phi = 0.25$.

The near-wall short-time dynamics at an intermediate volume fraction $\phi = 0.25$, represented by the initial decay rate, Γ, of the correlation function is shown in Figure 4. The data are plotted versus the parallel and perpendicular components of q for the quasi-perpendicular and quasi-parallel scans, respectively. In the quasi-perpendicular scan (Figure 4(a)), $q_{\parallel}$ (= 0.00884 nm^{-1}) is kept constant while

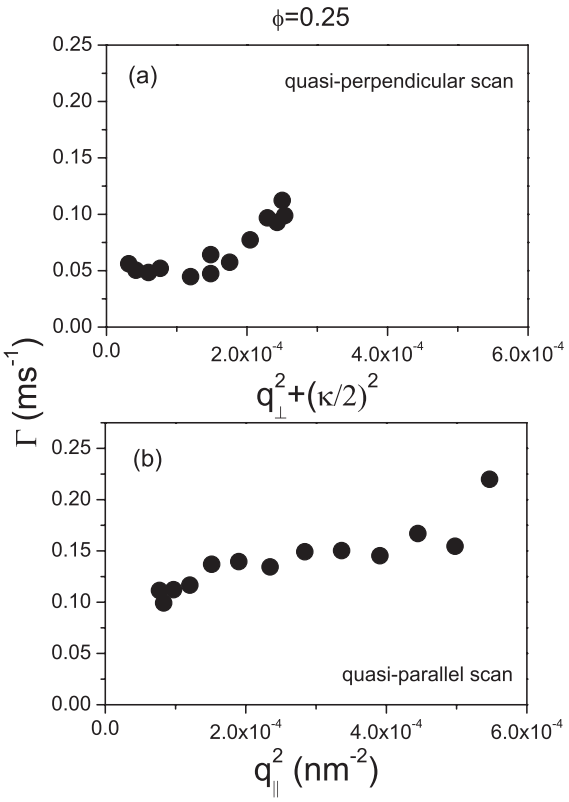

FIG. 4. (a) and (b) Initial decay rates from a quasi-perpendicular (with $q_\parallel = 0.00884$ nm^{-1}) and a quasi-parallel (with $q_\perp = 0.01531$ nm^{-1}) scan with the EWDLS2 setup $2/\kappa = 219$ nm ($\kappa R = 1.315$) at a volume fraction $\phi = 0.25$, as a function of $q_\perp^2 + \frac{\kappa^2}{4}$ and $q_\parallel^2$, respectively.

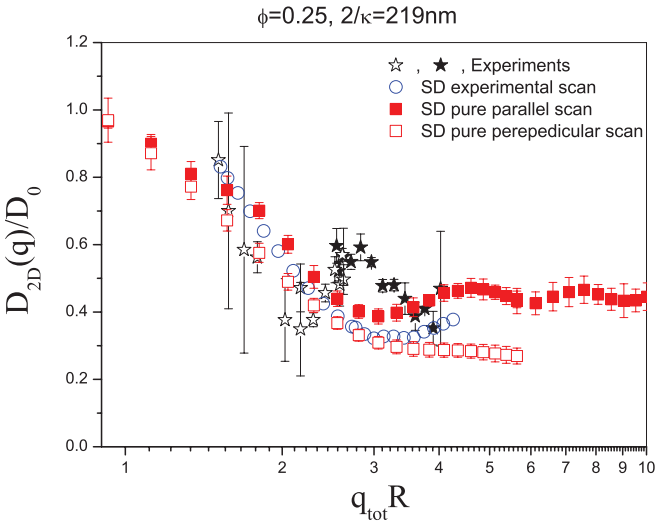

FIG. 5. Near wall (2D) normalized diffusion coefficients for a suspension with $\phi = 0.25$ as a function of $q_{tot}R$. Experimental quasi-perpendicular (solid stars, $q_\parallel = 0.00884$ nm^{-1}) and quasi-parallel (open stars, $q_\perp = 0.01531$ nm^{-1}) scan with $R = 144$ nm and $2/\kappa = 219$ nm ($\kappa R = 1.32$). SD simulation data from scans similar to the experiments (blue ◯) and for a pure perpendicular (red □, $q_\parallel = 0$) and a pure parallel (red ■, $q_\perp = 0$) scan are also shown.

$q_\perp$ ranges from 0.0033 nm^{-1} to 0.0153 nm^{-1}. In the quasi-parallel scan (Figure 4(b)), $q_\perp (= 0.0153$ nm$^{-1})$ is constant and $q_\parallel$ is varied from 0.0088 nm^{-1} to 0.0234 nm^{-1}. The dynamics are detected in the vicinity of the wall within a field penetration depth, $2/\kappa$, of about one particle diameter ($1/\kappa R = 0.76$). As suggested by Eq. (4), the initial slope, Γ, of the correlation function from the quasi-perpendicular (or quasi-parallel) scan have an almost linear dependence with $q_\perp^2 + \frac{\kappa^2}{4}$(or $q_\parallel^2$) with an intercept that represents $D_\parallel^s$ (or $D_\perp^s$). This behavior is similar to the anisotropic near-wall decay rates in dilute suspensions[28] and more recent simulation data at non-dilute volume fractions.[41] Below we compare the experimental data at the intermediate volume fraction, $\phi = 0.25$, as well as from a more concentrated suspension, $\phi = 0.42$, with Stokesian dynamics simulation data under the same conditions as the experiment, i.e., same penetration depth, $2/\kappa$, and scattering wave vectors, $q_\perp$ and $q_\parallel$.

In Figure 5, we plot the normalized near-wall diffusion coefficients, D_{2D}, deduced from the initial slope of the experimental correlation function from the two different scans (quasi-parallel and quasi-perpendicular, with EWDLS2 setup) at $\phi = 0.25$, as a function of $q_{tot}R$, with $q_{tot} = \sqrt{|\mathbf{k} \cdot \bar{\mathbf{k}}|} = \sqrt{q_\parallel^2 + q_\perp^2 + \frac{\kappa^2}{4}}$. For comparison, we include data from Stokesian dynamics simulations for the same $q_\perp$ and $q_\parallel$ with the experimental quasi-parallel and quasi-perpendicular scans as well as for a pure $q_\perp$ scan (with $q_\parallel = 0$) and a pure $q_\parallel$ scan (with $q_\perp = 0$). The experimental data from the two scans (quasi-parallel and quasi-perpendicular) match at an intermediate q_{tot} and correspond to a low q_{tot} regime (quasi-perpendicular scan) and a high q_{tot} regime (quasi-parallel scan), respectively. Since some of the data were taken under a varying, mixed homodyne-heterodyne conditions, the use of the modified Siegert relation introduces errors in the determination of the initial slope that could be significant in some cases as apparently seen around the minimum of $D_{2D}(\mathbf{q})$ in Figure 5. Nevertheless, the experimental data presented here show the expected q-dependent near-wall dynamics for a concentrated suspension,[16] i.e., a slowing down around the peak of structure factor, $S(\mathbf{q}) \equiv f(\mathbf{q}, 0; \kappa)$, and an increase at low q's, where the cooperative character of the diffusion is dominant. The latter is larger than the value of $D_{2D}(\mathbf{q})$ measured at high q's, beyond the peak of $S(\mathbf{q})$, where self-diffusion dynamics are probed. As we have seen before[16] in such concentrated suspensions, $D_{2D}(\mathbf{q})/D_0$ starts approaching $D_{3D}(\mathbf{q})/D_0$ essentially for all q's (see also Figure 6). Moreover, the experimental data match relatively well with the SD simulations taken with the same $q_\parallel$, $q_\perp$ and $2/\kappa$. The latter show more clearly the minimum of the $D_{2D}(\mathbf{q})/D_0$ around $q_{tot}R \sim 3.3$ where the $S(\mathbf{q})$ is expected to exhibit a peak.

Since both the quasi-perpendicular and quasi-parallel experimental scans were essentially performed keeping $q_\parallel$ and $q_\perp$ constant but finite (experimental conditions do not allow measurements with $q_\parallel = 0$ or $q_\parallel = 0$), we have performed the "pure" perpendicular and parallel scans with $q_\parallel = 0$ or $q_\perp = 0$, respectively, by SD simulations. Such scans allow us to probe the full anisotropy of the near-wall diffusivity. As we see in Figure 5 both pure scans exhibit a decreasing $D_{2D}(\mathbf{q})/D_0$ with increasing q, a result of qualitatively similar structural effects on the near-wall dynamics, represented by the static structure factor in the denominator of Eqs. (3)

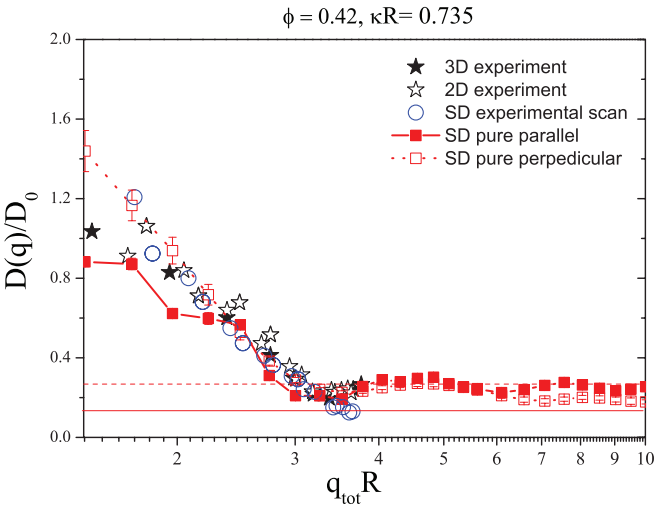

FIG. 6. Normalized diffusion coefficient as a function of total $q_{tot}R$ in bulk (3D, solid stars) and near wall (2D, open stars) for a mixed scan (EWDLS1) experiment with $R = 118$ nm, $2/\kappa = 321$ nm ($\kappa R = 0.735$) at a high volume fraction $\phi = 0.42$. SD simulation results with the same $q_{\parallel}$ and $q_{\perp}$ are also shown together with a pure parallel scan, $q_{\perp} = 0$, (red ■) and a pure perpendicular scan (red □). The high q-limit of $D_{\perp}^{S}$ is represented by the solid line and of the $D_{\parallel}^{S}$ by the dashed line.

and (7). In both the parallel and perpendicular directions, the cooperative diffusion at low q is faster than the self-diffusion measured at high q due to the increased osmotic compressibility of the suspension with increasing ϕ that speeds up the relaxation of long wavelength (low q) concentration fluctuations.[42,43] A closer look in Figure 5 shows that for low q's the near wall diffusivity, $D_{2D}(\mathbf{q})/D_0$, is almost identical in the parallel and the perpendicular directions, whereas at high q's $D_{2D}(\mathbf{q})/D_0$ is larger parallel than normal to the wall. We should note however that the low q range investigated here corresponds to values down to $q_{tot}R \sim 1$ and thus are far from the low-q thermodynamic limit. For the intermediate ϕ discussed here, the EWDLS cooperative diffusion measured at $q_{tot}R \sim 1$ is almost isotropic. On the other hand, the self-diffusion determined by EWDLS at high q's ($q_{tot}R > 4$) exhibits a clear anisotropy with the diffusion in the direction perpendicular to the wall slowing down more than in the parallel direction as expected from single particle-wall HI.[10,15,24,25]

In Figure 6, we show experimental 2D and 3D q-dependent diffusivities at a high volume fraction, $\phi = 0.42$, together with the corresponding SD simulation data. As shown in Ref. 16, at such high ϕ the near wall (2D) and the bulk (3D) short-time dynamics become nearly identical, for all q's as seen in Figure 6. SD simulations performed under the same conditions with experiment ($\kappa R = 0.735$ and same $q_{\parallel}, q_{\perp}$) are in very good agreement with EWDLS experimental data. Moreover, the SD pure parallel and perpendicular scans exhibit very similar $D_{2D}(\mathbf{q})/D_0$ suggesting that the near wall diffusion anisotropy is much weaker at high volume fractions compared to low and intermediate ϕ such as that shown in Figure 5. The larger differences between $D_{2D}^{\parallel}(\mathbf{q})$ and $D_{2D}^{\perp}(\mathbf{q})$ are detected in the limit of high and low q. For the self-diffusivity at high q, the component parallel to the wall is clearly higher than that perpendicular to the wall as the SD diffusivity data in the range $6 < q_{tot}R < 10$ show. This finding is in accordance with the true self-diffusivity limits indicated in Figure 6 by the dashed and solid lines, respectively. Hence, at $\phi = 0.42$ the self-diffusion is still anisotropic with the perpendicular component being slower than the parallel one. On the other hand, the mixed scan data performed at intermediate $q_{tot}R$ values and with $q_{\parallel}$ and $q_{\perp}$ of the same order are less sensitive in measuring the near wall diffusion anisotropy and do approach the 3D bulk dynamics.

At the same time, the low $q_{tot}R$ SD data exhibit some noteworthy features. The mixed experimental scan and corresponding SD data agree quite well both increasing at low q_{tot} due the drop of $S(\mathbf{q} \to 0)$. Regarding the pure scans, the diffusivity normal to the wall, $D_{2D}^{\perp}(\mathbf{q}, q_{\parallel} = 0)$ also increases at low $q_{tot}R$ following well the bulk data. On the other hand, the parallel component, $D_{2D}^{\parallel}(\mathbf{q}, q_{\perp} = 0)$, although it follows the perpendicular scan down to values of $q_{tot}R \approx 2$ it starts deviating from it for $q_{tot}R < 1.5$, suggesting that the cooperative diffusion might show a stronger anisotropy in the thermodynamic limit. However, one should recall that in the $qR \to 0$ limit $D_{2D}^{\parallel}(\mathbf{q}, q_{\perp} = 0)$ cannot be determined as Eq. (7) shows. As discussed above, this behavior is specific to the EWDLS averaging of near wall dynamics and indicates that the parallel to the wall collective hydrodynamics are too small in the $q_{\parallel}R \to 0$ limit and thus masked by perpendicular fluctuations due to the $\frac{\kappa}{2}\mathbf{e}_3$ term in $\mathbf{k}$. Therefore, in the $q_{\parallel} \to 0$ limit, both perpendicular and possibly cross terms are probed as well. The former essentially reflect number fluctuations in the scattering volume perpendicular to the wall defined by the penetration depth $2/\kappa$ that grow larger the smaller $q_{\perp}(2/\kappa)$ is, as pointed out at the early EWDLS studies.[10] Therefore, such a term is in principle important at all qR in the pure parallel scan and should be more evident when also $q_{\parallel} \to 0$. Moreover, it should be noted that the long-time tails in $f(\mathbf{q}, t; \kappa)$ are also related with such number fluctuations, especially in the dilute regime.[10]

We next discuss the volume fraction dependence of the EWDLS 2D self-diffusion coefficient, extracted experimentally at high q's and determined from SD simulations. Figure 7(a) shows experimental data from EWDLS measurements together with the corresponding bulk diffusivities from conventional DLS, all determined at $qR \simeq 4.6$ or higher where $S(\mathbf{q}) \sim 1$.[16,48] The experimental data correspond to those we presented previously in Ref. 16 using similar PMMA hard spheres with $R = 183$ nm for volume fraction up to $\phi = 0.36$ (using EWDLS1 setup with $2/\kappa = 800$ nm) while a $R = 154$ nm (EWDLS1 with $2/\kappa = 219$ nm) and $R = 118$ nm (EWDLS1 with $2/\kappa = 321$ nm) were also used for the two higher volume fractions, $\phi = 0.40$ and 0.42, respectively. We see that the experimental 3D and 2D diffusivities approach each other as ϕ is increased and are essentially indistinguishable for $\phi > 0.3$. SD simulations performed at the same penetration depths and several volume fractions in the $0.1 < \phi < 0.4$ range capture this trend quite well. Figure 7(a) depicts the parallel and perpendicular to the wall EWDLS self-diffusivities ($D_{2D}^{\parallel,s}$ and $D_{2D}^{\perp,s}$) from SD, as well as their average value. As expected, the parallel component, $D_{2D}^{\parallel,s}$, is larger than the perpendicular one, $D_{2D}^{\perp,s}$, and approaches

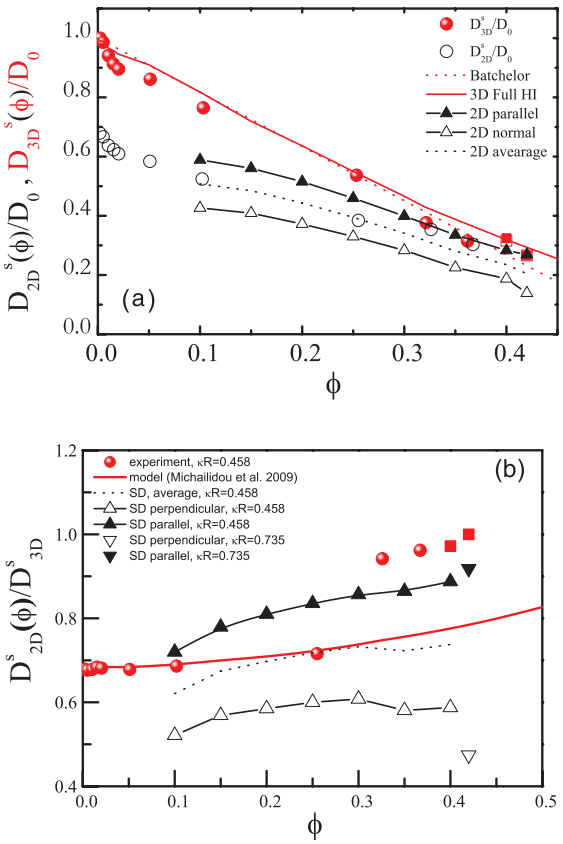

FIG. 7. (a) Normalized bulk (3D) and near wall (2D) self-diffusion coefficients from EWDLS experiments and SD simulations as indicated. Experimental data for $\phi < 0.36$ were gathered with EWDLS1 setup at $2/\kappa = 800$ nm using $R = 183$ nm (red open and solid circles). The two higher volume fraction data, $\phi = 0.4$ and $\phi = 0.42$, were taken at $2/\kappa = 321$ ($R = 154$ nm) and $2/\kappa = 321$ ($R = 118$ nm), respectively (red open and solid squares). Bulk data are compared with Batchelor's[50] (red dotted line) and SD with full HI calculations (red solid line).[44] SD simulation results corresponding to the pure perpendicular (open black triangle) and parallel (solid black triangle) EWDLS scans and their average, $D_{2D}^{av,s} = (D_{2D}^{\parallel,s} + D_{2D}^{\perp,s})/2$, (black dashed line) are also shown. (b) Volume fraction dependence of the ratio of EWDLS 2D to 3D self-diffusion coefficient corresponding to the data shown in Figure 7(a) determined experimentally at high q's for the data of Figure 7(a). The solid red line represents the simple model prediction by Michailidou *et al.* in Ref. 16.

earlier the bulk value, D_{3D}^s. The two pure components envelope the experimental data in the full ϕ range while their average, $D_{2D}^{av,s} = (D_{2D}^{\parallel,s} + D_{2D}^{\perp,s})/2$, is in very good agreement with experiments up to $\phi \sim 0.3$. At even higher volume fractions, the experimental data match better with the parallel to the wall diffusivity from SD simulations.

The ratio of the 2D to 3D self-diffusivity corresponding to the data of Figure 7(a) is depicted in Figure 7(b) both from experiments at high q and SD simulations. A simple model explaining the physical mechanism that masks the effects of wall HI on particle dynamics at high ϕ was proposed in Ref. 16. As we argued there, assuming that the particle-wall and particle-particle near-field (lubrication) HIs are the same, as they have the same singular behavior near contact, we can reasonably expect that at high concentrations and over short distances, a particle may not feel whether it is close to the wall or close to a second particle. We further assumed that the far-field contribution to the near-wall diffusivity has the same ϕ-dependence as in the bulk. Based on the above, we calculated the ratio of the 3D to the 2D short-time self-diffusivity with ϕ to be[16]

$$\frac{D_S^{3D}(\phi)}{D_S^{2D}(\phi,\kappa)} = 1 + \left(\frac{D_S^{3D}(\phi)}{D_{ff}^{3D}(\phi)}\right)\left(\frac{D_0}{D_0^{2D}(\kappa)} - 1\right), \qquad (11)$$

where the right hand side was determined using the experimental dilute limit ratio $D_0/D_0^{2D}(\kappa)$ while the ratio $D_S^{3D}(\phi)/D_{ff}^{3D}(\phi)$ was taken from simulations.[49] This simple model managed to capture qualitatively the approach of 2D and bulk dynamics evident in Figure 7(a). However, as seen in Figure 7(b) although the EWDLS experimental data agree with the simple model[16] quantitatively well up to $\phi \sim 0.3$, they indicate a significantly stronger approach with bulk dynamics at higher volume fractions. On the other hand, SD $D_{2D}^{av,s}/D_{3D}^s$ results underestimate the experimental data and seem to agree better with the simple model. For comparison, we also show SD results for a shorter penetration depth with $\kappa R = 0.735$ corresponding to the $\phi = 0.42$ experiment. It is evident that at shorter penetration depths the EWDLS averaging of the self-diffusion closer to the wall probe slower dynamics normal to the wall while the parallel component seems to be closer to the bulk dynamics. Therefore, the near wall diffusion anisotropy is still significant, even at volume fractions as high as $\phi = 0.42$, when in proximity to the wall.

Finally, in Figure 8 we show the SD data for the dilute limit EWDLS diffusivity and its $O(\phi)$ dependence. The free parallel and perpendicular diffusion coefficients, $D_{2D}^{\parallel}(\phi \to 0)$ and $D_{2D}^{\perp}(\phi \to 0)$,respectively, normalized to the Stokes-Einstein-Sutherland diffusion coefficient, D_0, were determined as a function of the penetration depth. SD simulations allowed us to determine the order ϕ volume fraction dependence of the average $D_{2D}^s(\phi,\kappa) = D_0^{2D}(\kappa)(1 - \alpha(\kappa)\phi)$ as well as of the parallel and perpendicular

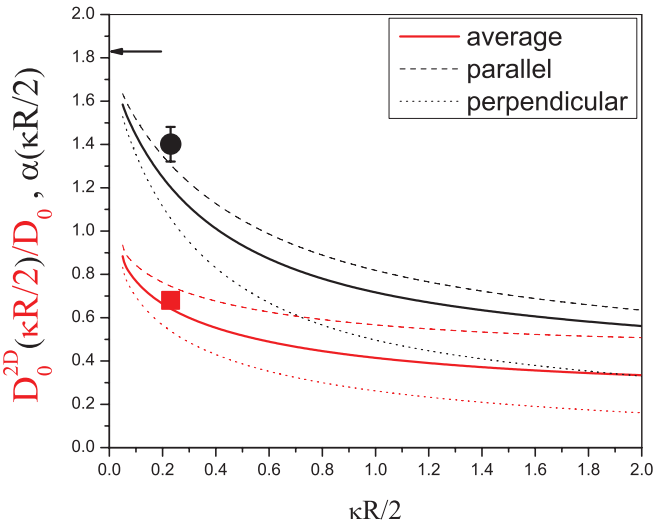

FIG. 8. SD results of the dilute limit EWDLS diffusivity normalized by the Stokes-Einstein-Sutherland diffusion coefficient, $D_0^{2D}(\kappa R/2)/D_0$, and the virial expansion (order ϕ) coefficient, $\alpha(\kappa R/2)$, as a function of penetration depth. The components parallel (dashed lines) and perpendicular (dotted lines) to the wall are shown together with their average (solid lines) values. The solid circle and square represent the experimental points for $\alpha(\kappa R/2)$ and $D_0^{2D}(\kappa R/2)/D_0$, respectively, while the arrow denotes the Batchelor prediction $\alpha = 1.83$.

components. Although in the bulk, Batchelor[50] predicts $\alpha(\kappa) = 1.83$, the EWDLS 2D experiments revealed a weaker decay (Figure 7(a)[16] with an $\alpha(\kappa)$ that depends on the penetration depth. The data deduced from the EWDLS experiments shown in Figure 7(a) (symbols in Figure 8) are in good agreement with SD predictions while both the diffusivities and $\alpha(\kappa)$ tend to the expected bulk values at $\kappa R \rightarrow 0$. Furthermore, Figure 8 shows that as the penetration depth decreases ($\kappa R/2$ increases) the diffusion anisotropy increases as $D_{2D}^{\parallel,s}$ and $D_{2D}^{\perp,s}$ diverge from each other and decrease in absolute values due to the enhanced hydrodynamic wall drag. Similarly, $\alpha(\kappa)$, being smaller for the perpendicular diffusion than for the parallel one, also decreases as one probes dynamics closer to the wall. The smaller near wall values of $\alpha(\kappa)$ extracted by SD simulations suggest that the wall screens out partly HIs among many particles in the dilute limit. This is reminiscent of the weaker decay of HIs near the wall following an $1/r^2$ dependence as compared to an $1/r$ dependence seen in the bulk.[16,51] This phenomenon affects more the perpendicular to the wall diffusivity, for which the HI may be as weak as $1/r^3$, leading to weaker order-ϕ dependence.

V. CONCLUSIONS

Here, we present a study of the dynamics of hard sphere particles near a hard wall as a function of volume fraction, from dilute to concentrated, and at a range of scattering wave vectors both below and above the peak of the structure factor. We have combined evanescent wave dynamic light scattering experiments that probe the near wall particle dynamics with Stokesian dynamics simulations that allow accurate determination of cooperative and self-diffusion dynamics properly taking into account the full hydrodynamic interactions. The results from experiments and simulations were discussed in view of an analytical theory that extended the conventional dynamic light scattering formalism taking into account the EWDLS near wall averaging of the dynamics to provide statistical quantities for the near wall diffusivities.[16,40]

As shown previously,[16] as the volume fraction is increased the near wall quasi-2D dynamics as probed both by EWDLS experiments and SD simulations approach the bulk (3D) dynamics due to a similitude of particle-wall and particle-particle HIs. Results from SD simulations reproduce well the experimental q-dependent diffusion coefficients at intermediate and at high volume fractions. SD simulations allowing us to probe the pure parallel and perpendicular components of $D_{2D}(\mathbf{q}, \kappa, \phi)$ suggest that near wall diffusion remains anisotropic even at high volume fractions especially at high q's where self-diffusion is probed, with the perpendicular component being slower than the parallel one. The latter approaches the bulk diffusivity earlier, i.e., at lower ϕ and smaller penetration depths. The average near wall dynamics deduced from SD simulations and predicted by a simple model are in very good agreement with experimental data for $\phi < 0.3$, but deviate from the latter at higher ϕ yielding a weaker proximity to the bulk dynamics compared to what is seen experimentally. Finally, a specific characteristic of the EWDLS probe of near wall dynamics related to the finite penetration depth prohibits approach to the low qR thermodynamic limit particularly in the parallel to the wall direction.

ACKNOWLEDGMENTS

We acknowledge funding from GSRT (THALES project, "Covisco"), European Union (EU) (Soft Matter Infrastructure project "ESMI"), and National Science Foundation (NSF) NIRT grant (CBET 0506701). We thank Andy Schofield for providing the colloids. We also thank Jan Dhont and Peter Lang for the hospitality provided to V.M. and the access to EWDLS2 setup (ICS-1, Forschungszentrum Juelich) during spring of 2009, as well as for many helpful discussions.

[1] J. Lyklema, *Fundamentals of Interface and Colloid Science* (Academic Press, 1995).
[2] Z. Adamczyk, *Principle at Interfaces, Interactions, Deposition, Structure* (Academic, 1998).
[3] I. H. Riedel, K. Kruse, and J. Howard, Science **309**, 300 (2005).
[4] A. Sokolov, I. S. Aranson, J. Kesslert, and R. E. Goldstein, Phys. Rev. Lett. **98**, 158102 (2007).
[5] G. M. Whitesides and A. D. Stroock, Phys. Today **54**(6), 42 (2001).
[6] D. Psaltis, S. R. Quake, and C. Yang, Nature (London) **442**, 381 (2006).
[7] D. A. Saville, W. B. Russel, and W. R. Schowalter, *Colloidal Dispersions* (Cambridge University Press, 1989).
[8] X. Ma, W. Chen, Z. Wang, Y. Peng, Y. Han, and P. Tong, Phys. Rev. Lett. **110**, 078302 (2013).
[9] R. Sigel, Curr. Opin. Colloid Interface Sci. **14**, 426 (2009).
[10] K. H. Lan, N. Ostrowsky, and D. Sornette, Phys. Rev. Lett. **57**, 17 (1986).
[11] G. Fytas, S. H. Anastasiadis, R. Seghrouchni, D. Vlassopoulos, J. B. Li, B. J. Factor, W. Theobald, and C. Toprakcioglu, Science **274**, 2041 (1996).
[12] E. Filippidi, V. Michailidou, B. Loppinet, J. Ruhe, and G. Fytas, Langmuir **23**, 5139 (2007).
[13] B. Loppinet, G. Petekidis, G. Fytas, R. Rulkens, and G. Wegner, Langmuir **14**, 4958 (1998).
[14] P. Holmqvist, J. K. G. Dhont, and P. R. Lang, Phys. Rev. E **74**, 021402 (2006).
[15] L. Lobry and N. Ostrowsky, Phys. Rev. B **53**, 12050 (1996).
[16] V. N. Michailidou, G. Petekidis, J. W. Swan, and J. F. Brady, Phys. Rev. Lett. **102**, 068302 (2009).
[17] M. D. Carabajal-Tinoco, R. Lopez-Fernandez, and J. L. Arauz-Lara, Phys. Rev. Lett. **99**, 138303 (2007).
[18] G. Volpe, T. Brettschneider, L. Helden, and C. Bechinger, Opt. Express **17**, 23975 (2009).
[19] M. Yoda and Y. Kazoe, Phys. Fluids **23**, 111301 (2011).
[20] M. A. Plum, W. Steffen, G. Fytas, W. Knoll, and B. Menges, Opt. Express **17**, 10364 (2009).
[21] M. A. Plum, B. Menges G. Fytas, H. J. Butt, and W. Steffen, Rev. Sci. Instrum. **82**, 015102 (2011).
[22] P. P. Lele, J. W. Swan, J. F. Brady, N. J. Wagner, and E. M. Furst, Soft Matter **7**, 6844 (2011).
[23] H. Faxen, Ark. Mat., Astron. Fys. **17**, 1 (1923).
[24] H. Brenner, Chem. Eng. Sci. **16**, 242 (1961).
[25] M. E. O'Neill, Mathematika **11**, 67 (1964).
[26] R. Jones, J. Chem. Phys. **123**, 164705 (2005).
[27] B. Lin, J. Yu, and S. Rice, Phys. Rev. E **62**, 3909 (2000).
[28] P. Holmqvist, J. K. G. Dhont, and P. R. Lang, J. Chem. Phys. **126**, 044707 (2007).
[29] S. A. Rogers, M. Lisicki, B. Cichocki, J. K. G. Dhont, and P. R. Lang, Phys. Rev. Lett. **109**, 098305 (2012).
[30] R. Pesche and G. Nagele, Phys. Rev. E **62**, 5432 (2000).
[31] T. Beatus, R. Bar-Ziv, and T. Tlusty, Phys. Rev. Lett. **99**, 124502 (2007).
[32] J. W. Swan and J. F. Brady, J. Fluid Mech. **687**, 254 (2011).
[33] E. R. Dufresne, T. M. Squires, M. P. Brenner, and D. G. Grier, Phys. Rev. Lett. **85**, 3317 (2000).
[34] B. X. Cui, H. Diamant, and B. H. Lin, Phys. Rev. Lett. **89**, 188302 (2002).
[35] B. Cui, H. Diamant, B. Lin, and S. Rice, Phys. Rev. Lett. **92**, 258301 (2004).
[36] D. T. Valley, S. A. Rice, B. Cui, H. M. Ho, H. Diamant, and B. Lin, J. Chem. Phys. **126**, 134908 (2007).

[37]J. Mittal, T. M. Truskett, J. R. Errington, and G. Hummer, Phys. Rev. Lett. **100**, 145901 (2008).
[38]J. Santana-Solano, A. Ramirez-Saito, and J. Arauz-Lara, Phys. Rev. Lett. **95**, 198301 (2005).
[39]C. R. Nugent, K. Edmond, H. N. Patel, and E. R. Weeks, Phys. Rev. Lett. **99**, 025702 (2007).
[40]J. W. Swan and J. F. Brady, J. Chem. Phys. **135**, 014701 (2011).
[41]B. Cichocki, E. Wajnryb, J. Blawzdziewicz, J. K. G. Dhont, and P. R. Lang, J. Chem. Phys. **132**, 074704 (2010).
[42]P. N. Pusey, in *Colloidal Suspensions in Liquids, Freezing and the Glass Transition*, Les Houches, Session LI, July 3–28, edited by J. P. Hansen, D. Levesque, and J. Zinn-Justin (Elsevier, Amsterdam, 1991).
[43]B. Berne and R. Pecora, *Dynamic Light Scattering with Applications to Chemistry, Biology and Physics* (Dover Publications, Inc., 2000).
[44]A. Sierou and J. F. Brady, J. Fluid Mech. **448**, 115 (2001).
[45]L. Durlofsky, J. F. Brady, and G. Bossis, J. Fluid Mech. **180**, 21 (1987).
[46]A. Donev, S. Torquato, and F. Stillinger, J. Comput. Phys. **202**, 737 (2005).
[47]M. Lisicki, B. Cichocki, J. K. G. Dhont, and P. R. Lang, J. Chem. Phys. **136**, 204704 (2012).
[48]P. N. Segre, O. P. Behrend, and P. N. Pusey, Phys. Rev. E **52**, 5070 (1995).
[49]A. J. Banchio and J. F. Brady, J. Chem. Phys. **118**, 10323 (2003).
[50]G. K. Batchelor, J. Fluid Mech. **74**, 1 (1976).
[51]J. W. Swan and J. F. Brady, Phys. Fluids **22**, 103301 (2010).